Available online at www.sciencedirect.com
SCIENCE DIRECT®
Journal of Sound and Vibration 269 (2004) 853–874
JOURNAL OF SOUND AND VIBRATION
www.elsevier.com/locate/jsvi

# Study of airfoil gust response alleviation using an electro-magnetic dry friction damper. Part 1: Theory

Deman Tang[a], Henri P. Gavin[b], Earl H. Dowell[a,*]

[a] *Department of Mechanical Engineering and Materials Science, Duke University, Box 90300, Durham, NC 27708-0300, USA*

[b] *Department of Civil Engineering, Duke University, Box 90300, Durham, NC 27708-0300, USA*

Received 19 August 2002; accepted 9 January 2003

**Abstract**

An electro-magnetic controllable dry friction damper has been designed and numerically simulated. The gust response of a three degree-of-freedom typical airfoil section with a control surface using this non-linear damper has been studied theoretically. The effects of the different gust excitations and parameter variations of the non-linear damper on the non-linear aeroelastic response are discussed. The numerical results show the present electro-magnetic dry friction damper can be used to alleviate the dynamic response to both a periodic and a linear frequency sweep gust excitation, especially for the plunge and pitch responses. The results are also verified by an experimental investigation in a wind tunnel presented in a companion paper, Part 2.



## 1. Introduction

Recently, several types of semi-active electrorheological (ER) or magnetorheological (MR) dampers have been used for vibration attenuation of various dynamical systems. It has been shown that these dampers, when combined with appropriate control strategies, can be used to achieve improved performance of the dynamical system [1–3]. The design and applications of MR devices have been an area of recent interest due to the controllable characteristics of MR materials. Ref. [4] demonstrated how some of the key characteristics of MR fluids can be improved, such as increasing their yield stress, thereby permitting a wider variety of applications. Refs. [5–8] described work on modelling the dynamic characteristics of MR devices through a

*Corresponding author.
*E-mail address:* dowell@mail.ee.duke.edu (E.H. Dowell).

0022-460X/03/$ - see front matter © 2003 Elsevier Ltd. All rights reserved.
doi:10.1016/S0022-460X(03)00180-9

variety of approaches. New approaches to developing MR devices are being explored and new designs are being tested, e.g., Refs. [9,10]. Also there are several important patents on MR devices.

However, for most ER or MR dampers, the structural parameters of the dampers, such as cylinder piston, magnetic flux and coil masses and the magnetic flux shear stiffness, significantly change the characteristics of the dynamical system. Another property of these dampers is the dry friction force caused by the seal ring. This force has almost a constant value and is per se uncontrollable.

The present MR damper design follows that of Ref. [11], although we did not use a magnetic flux with the fluid material to form the magnetic circuit. A simple damping device is constructed to generate a controllable dry friction force in an aeroelastic model. This damping device is called an electro-magnetic dry friction damper (EMD). The EMD device provides a non-linear dry friction damping force which can be represented by

$$f_D = f_d(I)\tanh\left(\frac{\dot{h}}{v_0}+\frac{h}{d_0}\right),$$

where $f_d(I)$ is an experimentally determined dry friction force amplitude which is dependent upon the current ($I$) of the EMD magnetic circuit and $h$ and $\dot{h}$ are the input displacement and velocity variables.

A theoretical/experimental study of the self-excited aeroelastic response of a three degree-of-freedom (d.o.f.) typical airfoil section with a freeplay in the control surface and non-linear stiffness in plunge or torsion directions has been made by the Duke team as well as other investigators [12]. For a summary of the literature on non-linear aeroelasticity and corresponding references, see Ref. [13]. Here, a first theoretical (Part 1)/experimental (Part 2) study of the non-linear aeroelastic response to a gust excitation for a three d.o.f. typical airfoil with an electro-magnetic dry friction damper is conducted. The theoretical aerodynamic forces are obtained from Peters' finite-state airloads model, see Ref. [14]. In the present paper a time-domain computer simulation method proposed in Ref. [15] is extended to calculate non-linear gust response when the time-correlated gust loads are known. Of course, the Peters' finite-state airloads model considers the effect of gust loads on the aerodynamics as well as the motion-induced aerodynamics. Sinusoidal and linear frequency sweep gust loads are used. The present theoretical results may be helpful in better understanding physically the alleviation of a typical airfoil section response due to gust loads using an electro-magnetic dry friction damper.

## 2. Numerical model and controllable EMD damper

The numerical (and experimental) model consists of a two-dimensional NACA 0012 rectangular wing model mounted on support mechanisms including the EMD dampers which are placed outside of the wind tunnel. The wing model includes two parts: a main wing and a control surface or flap which is attached at the trailing edge of the main wing. The pitch axis of the main wing is located at the quarter-chord. The support mechanism at each end of the rectangular wing is a bi-cantilevered beam which provides the plunge stiffness. Two EMD dampers are symmetrically mounted on both the top and bottom of the wind tunnel and the output end of each

EMD damper is connected to the free end of the bi-cantilever beam through a steel plate and the magnetic powder. A schematic of the experimental model is shown in Fig. 1.

The configuration of the EMD damper is shown in Fig. 2(a). The damping device consists of three parts: the first is an electro-magnetic generator caused by a spool wire in a low-carbon steel bar with two low-carbon steel blocks at the bar ends. The second is a low-carbon steel plate which is fixed to the plunge spring system of the aeroelastic model. There is a gap between the steel blocks of the electro-magnetic generator and the steel plate. The third is the special magnetic material powder (carbonyl iron powder) which fills the gap. The carbonyl iron powder (BASF #819011, Mount Olive, NJ) is mono-disperse with a mean diameter of about five microns. In this system, a controllable dry friction force can be obtained that depends upon the dimensions of the damping device and the input current. The basic principle for the controllable dry friction force is shown in Fig. 2(b). When no magnetic field acts, the powder (magnetic cell) is randomly dispersed in the gap as given in Part 1; a small dry friction force is provided by the dry friction between the magnetic powder and the steel surfaces. When the magnetic field acts, the powder aggregates like a "bent-wall" as shown in Part 2. Therefore, the layered shear friction in the powder itself and also between the powder and the steel surfaces increases. How much it increases depends upon the driving current and the structural parameters of the damping device.

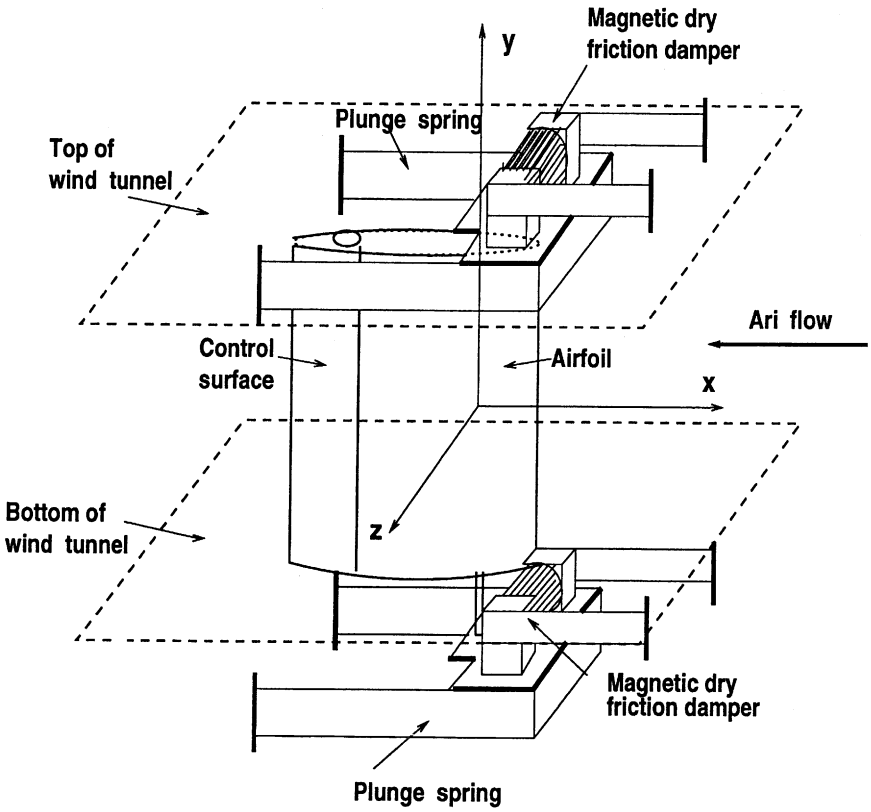


Fig. 1. Schematic of the aeroelastic model in the wind tunnel.

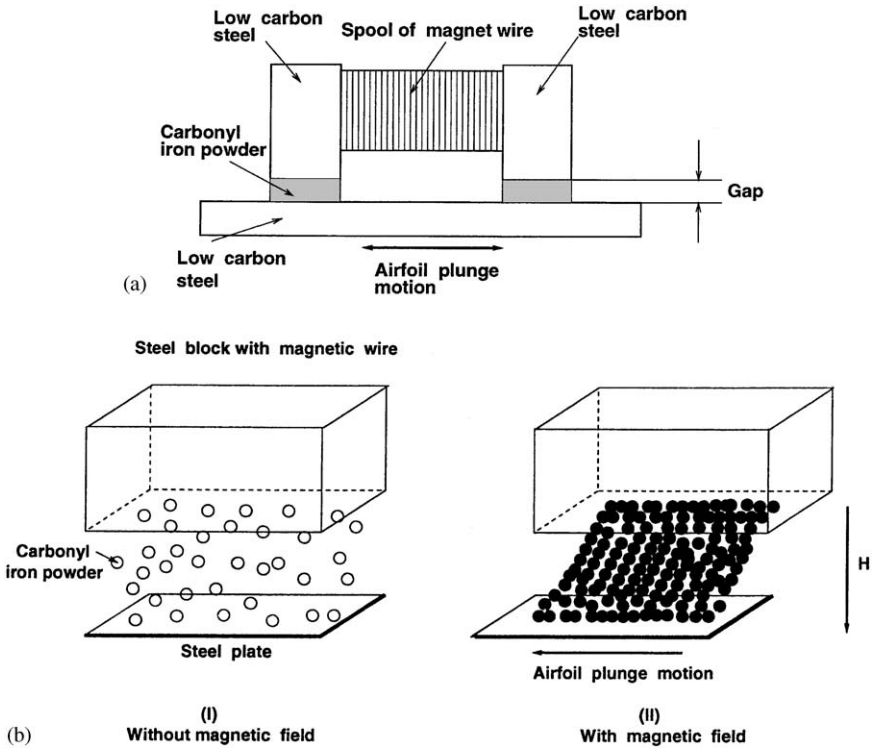


Fig. 2. (a) EMD damper configuration and (b) basic theoretical model.

## 3. Gust loads

Atmospheric turbulence creates a gust load which can be represented by two different mathematical descriptions. One is associated with a discrete gust representation usually of a deterministic nature. On the other hand, continuous turbulence can be represented by a stochastic process. In the present work, a discrete gust representation is used.

In general, atmospheric turbulence is considered to be a function of three spatial dimensions and time. In this paper, the atmospheric turbulence velocity field is composed of only a lateral component and the frozen gust assumption is used [16]. For the frozen gust, the gust field is given by

$$w_g(x') = w_g(x - Ut),$$

where $x, t$ are co-ordinates fixed with respect to airfoil and $x', t'$ are co-ordinates fixed with respect to the fluid atmosphere.

Since $x$ and $t$ only appear in the above combination, we may consider the alternative functional form

$$w_g = w_g\left(t - \frac{x}{U}\right).$$

Following thin airfoil theory, the lateral gust velocity is expanded as

$$w_g = \sum_{n=0}^{\infty} w_{gn} \cos(n\phi), \tag{1}$$

where $\phi = \cos^{-1}(x/b)$.

We assume that at $t = t_0$, the leading-edge of airfoil has a gust velocity

$$w_{gl} = w_g\left(t_0 + \frac{b}{U}\right) \quad (x = -b),$$

and at the trailing-edge of airfoil the gust velocity is

$$w_{gt} = w_g\left(t_0 - \frac{b}{U}\right) \quad (x = b).$$

If the gust is known as a discrete time series with a constant sampling time step length, $\Delta t$, the gust at any chordwise position of the airfoil ($x_j$) is

$$w_{gc}(t_0) = w_g\left(t_0 + \frac{x_j}{U}\right) = w_g(t_0 + j\Delta t),$$

where $j$ is an integral number starting from the leading-edge ($j = 1$) and ending at the trailing-edge ($j = n_s$), $n_s = 2b/U\Delta t$.

At $t = t_0$, the $w_{gn}$ coefficients of Eq. (1) can be determined by

$$w_{g0}(t_0) = \frac{1}{\pi}\int_0^{\pi} w_{gc}(t_0, x)\,\mathrm{d}\phi = \frac{1}{\pi}\int_{-b}^{b} \frac{w_{gc}(t_0)}{b\sin(\cos^{-1}(x/b))}\,\mathrm{d}x = \frac{1}{b\pi}\sum_{j=1}^{n_s} \frac{w_{gc}(t_0, x_j)\Delta x}{\sin(\cos^{-1}\phi_j)}, \tag{2}$$

where $\Delta x = U\Delta t$, $x_j = j\Delta x$ and $\phi_j = (x_j - b)/b$, and

$$w_{gn}(t_0) = \frac{2}{\pi}\int_0^{\pi} w_{gc}(t_0, x)\cos n\phi\,\mathrm{d}\phi = \frac{2}{b\pi}\sum_{j=1}^{n_s} \frac{w_{gc}(t_0, x_j)\cos(n\cos^{-1}\phi_j)\Delta x}{\sin(\cos^{-1}\phi_j)}. \tag{3}$$

Thus, $w_{g0}(t_0)$ and $w_{gn}(t_0)$ can be determined using a standard numerical integration code. When we use a time integral method to solve the non-linear state equations of motion, those coefficients are evaluated at each time step.

In this paper, two special gusts are used. One is a continuous sinusoidal gust. It is expressed as

$$w_g(t) = \bar{w}_{gs}\sin\omega t, \tag{4}$$

where $\omega$ is the gust excitation frequency. The other is a continuous frequency sweep gust and it is expressed as

$$w_g(t) = \bar{w}_{gs}\sin\left(\omega_1 + \frac{\omega_2 - \omega_1}{2T}t\right)t, \tag{5}$$

where $\omega_1, \omega_2$ and $T$ are the minimum frequency, maximum frequency, and the sweep duration respectively.

For a sinusoidal gust, the $w_{gn}$ coefficients of Eq. (1) are determined by

$$w_{g0}(t_0) = \frac{1}{\pi}\int_0^{\pi} \bar{w}_{gs}\sin(\omega t - \Delta\psi)\,\mathrm{d}\phi = \frac{\bar{w}_{gs}}{b\pi}[C_0\sin\omega t - S_0\cos\omega t], \tag{6}$$

where

$$C_0 = \sum_{j=1}^{n_s} \frac{\cos \Delta\psi \Delta x}{\sin(\cos^{-1} \phi_j)}, \qquad S_0 = \sum_{j=1}^{n_s} \frac{\sin \Delta\psi \Delta x}{\sin(\cos^{-1} \phi_j)},$$

and for $n \geqslant 1$,

$$w_{gn}(t_0) = \frac{2}{\pi} \int_0^{\pi} \bar{w}_{gs} \sin(\omega t - \Delta\psi) \cos n\phi \, \mathrm{d}\phi = \frac{2\bar{w}_{gs}}{b\pi} [C_n \sin \omega t - S_n \cos \omega t], \tag{7}$$

where

$$C_n = \sum_{j=1}^{n_s} \frac{\cos \Delta\psi \cos(n \cos^{-1} \phi_j) \Delta x}{\sin(\cos^{-1} \phi_j)}, \qquad S_n = \sum_{j=1}^{n_s} \frac{\sin \Delta\psi \cos (n \cos^{-1} \phi_j) \Delta x}{\sin(\cos^{-1} \phi_j)},$$

and $\Delta\psi$ is a phase difference which is defined as $\Delta\psi = x_j/l_g$ and $l_g$ is the gust wavelength which is defined as $l_g = U/\omega$. Note that the integral terms, $C_0$, $C_n$, $S_0$ and $S_n$ do *not* need to be evaluated at each time step.

## 4. State-space theoretical model

A schematic of a typical airfoil section with an electro-magnet dry friction damper is shown in Fig. 1. The aeroelastic typical section has three d.o.f. plunge ($h$), torsion ($\alpha$) of the main wing and rotation ($\beta$) of the control surface about the point, c.

The differential equations of structural motion expressing the equilibrium of the moments about point $a$ of the entire airfoil, of the moments on the control surface about point $c$, and of the vertical forces on the airfoil are as follows:

$$\begin{aligned}
&I_\alpha \ddot{\alpha} + I_\beta \ddot{\beta} + b(c-a) S_\beta \ddot{\beta} + S_\alpha \ddot{h} + C_\alpha \dot{\alpha} + K_\alpha \alpha = M_\alpha,\\
&I_\alpha \ddot{\alpha} + I_\beta \ddot{\beta} + I_\alpha \ddot{\alpha} + b(c-a) S_\beta \ddot{\alpha} + S_\beta \ddot{h} + C_\beta \dot{\beta} + K_\beta \beta = M_\beta,\\
&M\ddot{h} + S_\alpha \ddot{\alpha} + S_\beta \ddot{\beta} + C_h \dot{h} + K_h h = L - f_D \delta(y - l/2) - f_D \delta(y + l/2),\\
&f_D = f_d(I) \tanh\left(\frac{\dot{h}}{v_0} + \frac{h}{d_0}\right).
\end{aligned} \tag{8}$$

Note that the damper forces act at the wing elastic axis.

Eq. (8) may be expressed in a compact matrix form as

$$[M_s]\{\ddot{y}\} + [C_s]\{\dot{y}\} + [K_s]\{y\} = [S_1](\{F_a\} - \{F_N\}), \tag{9}$$

where $\{y\}$ is expressed as $\{h, \alpha, \beta\}^{\mathrm{T}}$, $\{F_N\} = \{f_d(I) \tanh(\dot{h}/v_0 + h/d_0)/l, 0, 0\}^{\mathrm{T}}$,

$$[S_1] = \begin{bmatrix} 1/M_r b & 0 & 0 \\ 0 & 1/M_r b^2 & 0 \\ 0 & 0 & 1/M_r b^2 \end{bmatrix},$$

$$[K_s] = \begin{bmatrix} K_h & 0 & 0 \\ 0 & K_\alpha & 0 \\ 0 & 0 & K_\beta \end{bmatrix},$$

and $[C_s]$ is the structural damping matrix. An attempt has been made here to include structural damping in the theoretical model in a logical and physically meaningful way using viscous modal damping coefficients, see Ref. [15].

The non-linear damping force $f_d(I)$ is the yield force and is the only parameter controlled by the input current.

The right side of Eq. (8) forms a vector of aerodynamic forces, $\{F_a\} = \{L, M_\alpha, M_\beta\}^{\mathrm{T}}$. We use Peters' finite-state incompressible airloads model for a deformable airfoil [14] to determine these aerodynamic forces in a matrix form. They are

$$[S_1]\{F_a\} = \lambda_0\{P\} - [K_a]\{y\} - [C_a]\{\dot{y}\} - [M_a]\{\ddot{y}\} + [G_1]\{w_{gn}\} + [G_2]\{\dot{w}_{gn}\}. \tag{10}$$

For matrices $\{P\}, [K_a], [C_a], [M_a]$, see Ref. [14] and for $[G_1], [G_2]$ see Ref. [17].

An approximate $\lambda_0$ is determined by

$$\lambda_0 \approx \frac{1}{2}\sum_{n=1}^{N} b_n\lambda_n. \tag{11}$$

The closed-form expressions for the $b_n$ are given in Ref. [18, Appendix C].

The inflow, $\lambda_n$, can be determined by an inflow matrix equation (see Ref. [18]). It is

$$[A]\{\dot{\lambda}\} + \frac{U}{b}\{\lambda\} = [B_1]\{\ddot{y}\} + \frac{U}{b}[B_2]\{\dot{y}\} + [B_g]\{\dot{w}_{gn}\}, \tag{12}$$

where the matrix $[A]$ is given in Ref. [18] and $[B_1], [B_2], [B_g]$ is given in Ref. [17].

Eq. (12) is basically an equation for the time evolution of vortex transport in the wake of the airfoil. Combining Eqs. (8)–(12), and defining $X_e = \{\dot{y}, y, \lambda\}^{\mathrm{T}}$, we obtain a set of state-space equations with six structural states and $N$ inflow states. These equations are

$$\dot{X}_e = A_e X_e + B_e, \tag{13}$$

where

$$A_e = \begin{bmatrix} M_e & C_e & 0 \\ 0 & M_e & 0 \\ -B_1 & -\frac{U}{b}B_2 & A \end{bmatrix}^{-1} \begin{bmatrix} 0 & -K_e & B_n \\ M_e & 0 & 0 \\ 0 & 0 & -\frac{U}{b}I \end{bmatrix},$$

$$B_e = \begin{bmatrix} M_e & C_e & 0 \\ 0 & M_e & 0 \\ -B_1 & -\frac{U}{b}B_2 & A \end{bmatrix}^{-1} \left( \begin{Bmatrix} -F_d \\ 0 \\ 0 \end{Bmatrix} + [G_{e1}]\{w_{gn}\} + [G_{e2}]\{\dot{w}_{gn}\} \right),$$

and where sub-matrices $M_e$, $K_e$ and $C_e$ are the equivalent mass, stiffness and damping matrices comprised of structural and aerodynamic components, $M_e = [M_s] + [M_a]$, $C_e = [C_s] + [C_a]$, $K_e = [K_s] + [K_a]$ and the sub-matrices, $B_n, G_{e1}, G_{e2}$, are given in Ref. [17].

## 5. Numerical results

The parameters of the numerical model come from the experimental model previously described in Ref. [15]. The nominal values for the inertial, stiffness, and damping parameters of the

experimental structural system were measured. A summary of the system parameters is given in Table 1. The theoretical structural natural frequencies (without the EMD damping device) are $\omega_\alpha = 7.91$ Hz, $\omega_\beta = 17.08$ Hz and $\omega_h = 4.07$ Hz. Two sets of the EMD damper parameters are included in the numerical study, i.e., $v_0 = 0.13$ cm/s, $d_0 = 0.024$ cm, and $v_0 = 2.2$ cm/s, $d_0 = 0.08$ cm. The damping force $f_d$ varies from 0 to 2.0 N depending on the input current.

### 5.1. Non-linear damping force of EMD damper

The non-linear damping force of EMD damper can be represented by

$$f_D = f_d(I)\tanh\left(\frac{\dot{h}}{v_0} + \frac{h}{d_0}\right). \tag{14}$$

The non-linear damping force of the EMD damper as described by Eq. (14) is shown in Fig. 3 for $f_D$ vs. $\dot{h}$ and $f_D$ vs. $h$. In this figure, the input displacement, $h$, is a sinusoidal motion. The sinusoidal excitation frequency and amplitude are chosen as 5 Hz and 0.005 m, respectively. Three different input currents, $I_1, I_2$ and $I_3$ corresponding to $f_d(I) = 1, 5, 10$ N are applied to the EMD damper for $v_0 = 0.13$ cm/s, $d_0 = 0.024$ cm. The output damping force has a hysteretic behavior and the damping force level increases as the input current $I_i$ increases.

The non-linear damping force behavior also depends on the parameters $v_0$ and $d_0$ for a fixed input current, $I$. When the input is a single harmonic motion with an amplitude, $h_s = 0.5$ cm, and a frequency, $\omega = 5$ Hz, the parameters are chosen to be $f_d = 6$ N and $d_0 \to \infty$, say $d_0 = 10^5$ cm. Several $v_0$ were considered with a nominal value of $v_0 = 0.13$ cm/s. However $10 \times v_0$, $50 \times v_0$ and $100 \times v_0$ were also studied. The results are shown in Fig. 4. It is seen that the hysteretic behavior

Table 1
Various parameters

| | |
|---|---|
| Span (l) | 0.52 m |
| Semi-chord (b) | 0.127 |
| Elastic axis (a) | −0.0625 m |
| Hinge line (c) | 0.0625 m |
| Mass of wing | 0.713 kg |
| Mass of aileron | 0.18597 kg |
| Mass/length of wing-aileron | 1.73 kg/m |
| (Mass of support blocks) | (0.586 × 2 kg) |
| $I_\alpha$ (per span) | 0.0185 kg m |
| $I_\beta$ (per span) | 0.000254 kg m |
| $S_\alpha$ (per span) | 0.0726 kg |
| $S_\beta$ (per span) | 0.00395 kg |
| $K_\alpha$ (per span) | 42.8 kg m/s$^2$ |
| $K_\beta$ (per span) | 3.3 kg m/s$^2$ |
| $K_h$ (per span) | 2755.4 kg m/s$^2$ |
| $\zeta_\alpha$ (half-power) | 0.0175 |
| $\zeta_\beta$ (half-power) | 0.016 |
| $\zeta_h$ (half-power) | 0.012 |

becomes more evident when $v_0$ increases, but the damping force level decreases. Similar results are obtained for the nominal parameters $v_0 \to \infty$, say $v_0 = 10^5$ cm/s and $d_0 = 0.024$ cm when $d_0$ is increased to $100 \times d_0$. The results are shown in Fig. 5.

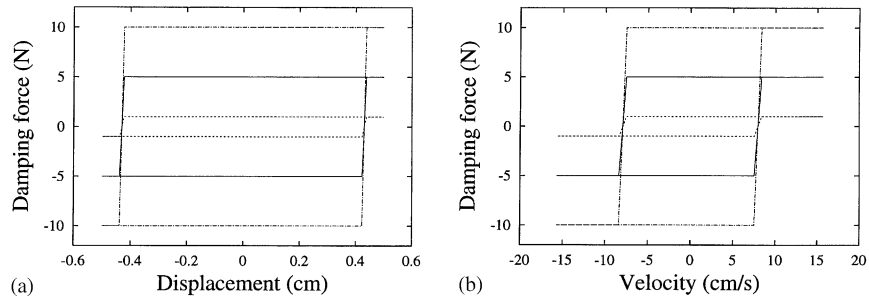


Fig. 3. Non-linear damping force characteristics for three different input currents: (a) damping force vs. displacement, (b) damping force vs. velocity.

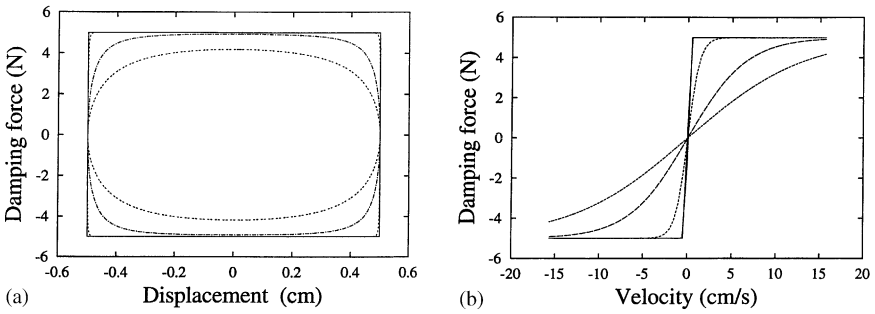


Fig. 4. Non-linear damping force characteristics for different parameters, $v_0$, in the open-loop system: (a) damping force vs. displacement, (b) damping force vs. velocity; —, $v_0 = 0.13$ cm/s; ···, $10v_0$; ---, $50v_0$; - -, $100v_0$.

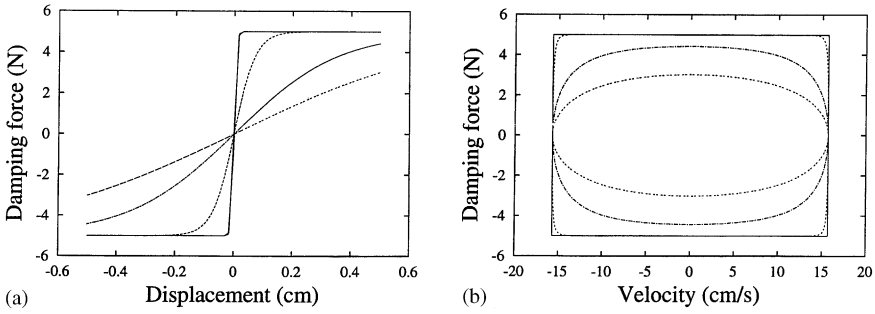


Fig. 5. Non-linear damping force characteristics for different parameters, $d_0$, in the open-loop system: (a) damping force vs. displacement, (b) damping force vs. velocity; —, $d_0 = 0.024$ cm; ···, $10d_0$; ---, $50d_0$; - -, $100d_0$.

### 5.2. Stability of the linear aeroelastic model

When the non-linear damping force $F_N$ in Eq. (13) is set to zero, a linear aeroelastic model is obtained. The aeroelastic eigenvalues obtained from solving these equations determine the stability of the system. When the real part of any one eigenvalue, $\lambda$, becomes positive, the entire system becomes unstable.

Figs. 6(a) and (b) show a typical graphical representation of the eigenanalysis in the form of real eigenvalues $\mathrm{Re}(\lambda_i)$ (aeroelastic damping) vs. the flow velocity and also a root-locus plot for the linear system. There is an intersection of $\mathrm{Re}(\lambda_i)$ with the velocity axis at $U_f = 28.6$ m/s, the critical flutter velocity, as shown in Fig. 6(a) with a corresponding flutter oscillatory frequency, $\omega_f = 5.56$ Hz, as shown in Fig. 6(b).

### 5.3. Non-linear response to single harmonic gust load (Case 1)

We have used a standard Runge–Kutta algorithm in conjunction with Peters' aerodynamic model, Eq. (13), for time integration of the non-linear equations. The flow velocity is chosen as $U = 18$ m/s, lower than the flutter velocity. The peak gust angle of attack is $\alpha_g = 1^\circ$ and the lateral peak gust velocity is $w_g = U\alpha_g/57.3$. The EMD damper parameters are $v_0 = 0.13$ cm/s, $d_0 = 0.024$ cm and $f_d = 0$, 0.5, 1.0 and 2 N. The results are shown in Fig. 7 for the plunge, pitch and flap rotation r.m.s. amplitude vs. the gust excitation frequency. As shown in Fig. 7(a), the plunge resonant frequency is 4.58 Hz. When no EMD damper is included in the system, i.e., $f_d = 0$, the plunge resonant r.m.s. amplitude is 1.1 cm, the corresponding pitch r.m.s. amplitude is $1.2^\circ$ and the flap rational angle is $0.68^\circ$ as shown in Figs. 7(b) and (c), respectively. The pitch resonant frequency is 7.4 Hz and flap resonant frequency is 17 Hz. When $f_d = 0.5$ N, the plunge resonant frequency is still 4.58 Hz, but the r.m.s amplitude decreases to 0.59 cm. The corresponding pitch and flap responses are also decreased at this frequency from $1.2^\circ$ to $0.67^\circ$ and $0.68^\circ$ to $0.37^\circ$. However, there are slight increases of their resonant frequencies. When $f_d = 1.0$ N, the plunge response has been significantly alleviated in the dominant resonant range. Also the pitch and flap rotation responses show alleviation except for the flap response at the flap resonant frequency. When $f_d = 2.0$ N, the plunge motion "sticks". The plunge d.o.f. of the

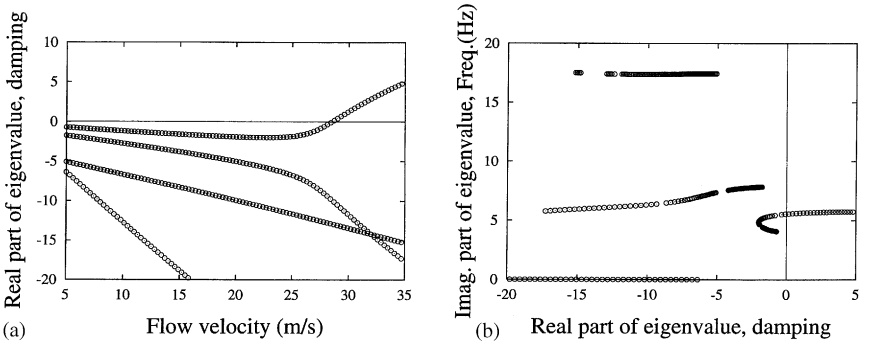


Fig. 6. Stability analysis of the linear aeroelastic model: (a) for real part of eigenvalue, (b) for root-locus.

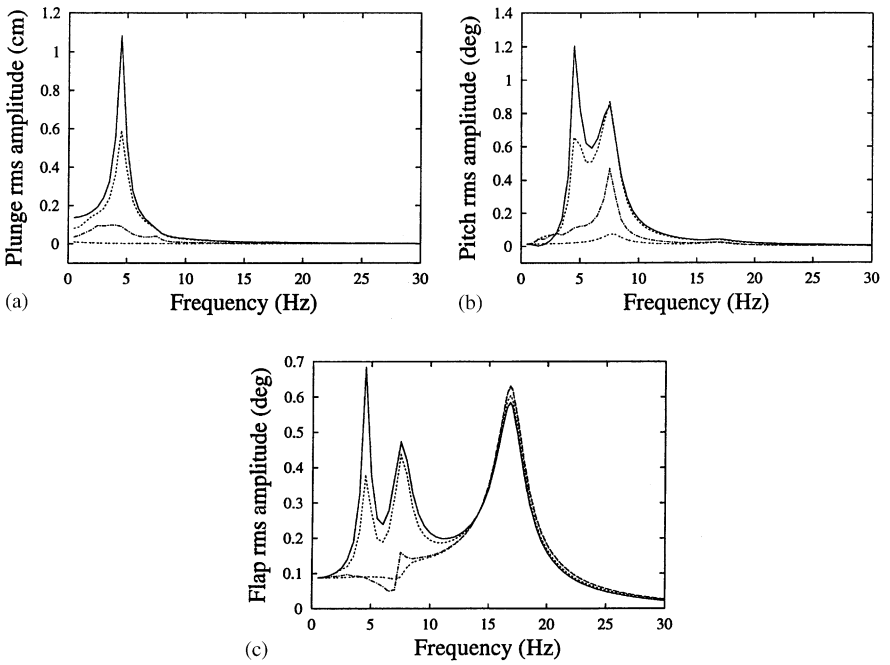


Fig. 7. R.m.s. frequency response vs. the gust excitation frequency: (a) for plunge, (b) for pitch and (c) for flap response; —, $f_d = 0$ N; ⋯, $f_d = 0.5$ N; ---, $f_d = 1.0$ N; - -, $f_d = 2.00$ N.

dynamic system is constrained. The pitch resonant frequency has slightly increased, i.e., from 7.4 to 7.5 Hz. The pitch resonant amplitude is significantly decreased. The flap peak responses disappear at frequencies, 4.58 and 7.4 Hz, and slightly increases at frequency 17 Hz.

Fig. 8 shows the plunge, pitch and flap rotation time histories at frequencies 4.5, 7.4 and 17 Hz, respectively, for several EMD damping force levels. The response motions are basically single harmonic with some higher harmonic content for the higher levels of damping forces.

Now consider the effects of the EMD damper parameters on the gust response. The damper parameters are $v_0 = 0.13$ cm/s, $d_0 = 0.024$ cm or $v_0 = 2.2$ cm/s, $d_0 = 0.08$ cm. The gust load is the same as before. Fig. 9 shows the gust response using the two sets of the damper parameters for the frequency $\omega = 4.5$ Hz and $f_d = 1$ N. The form of the dry friction damping forces are somewhat different when $d_0$ and $v_0$ increase, i.e., the force hysteretic behavior is changed, but the force amplitudes are the same. The gust responses are shown in Fig. 10. Fig. 10(a) shows the plunge response vs. time. The dashed line is the result obtained for the second set of damper parameters. The response motion is more like a sinusoid; this is because the EMD damper force is more like a sinusoid than a square wave; see Fig. 9. Also the response amplitude increases because the new damper parameters provides less dry friction force in an oscillation cycle; see Fig. 9. From Fig. 10(a) it is also seen that there is a phase angle shift between two results. Fig. 10(b) shows the damping force vs. plunge response.

A similar result is shown in Fig. 11 for the pitch response vs. time.

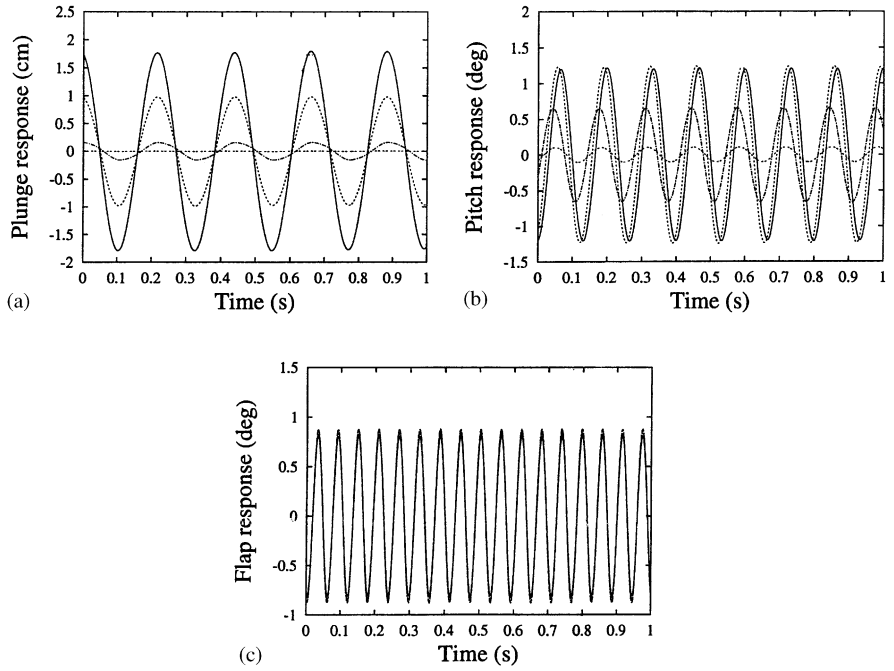


Fig. 8. Time history behavior: (a) for plunge response at $\omega = 4.5$ Hz, (b) for pitch response at $\omega = 7.4$ Hz, and (c) for flap response at $\omega = 17$ Hz; —, $f_d = 0$ N; ⋯, $f_d = 0.5$ N; ---, $f_d = 1.0$ N; - -, $f_d = 2.00$ N.

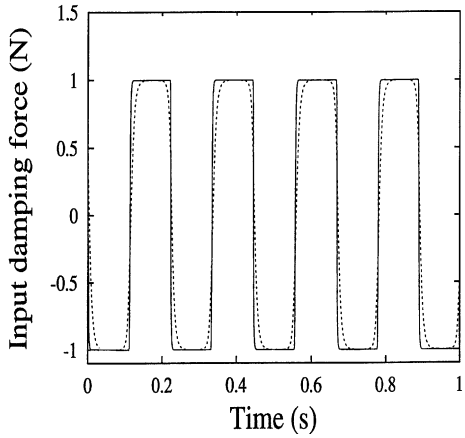


Fig. 9. Input damping force for different EMD damper parameters.

When the damping force amplitude, $f_d$ decreases from $f_d = 1$ to 0.5 N, the effect of the EMD damper parameter on the gust response decreases. The results are shown in Fig. 12. Thus, all the damper parameters, $f_d$, $d_0$ and $v_0$, are important for the alleviation of the gust response.

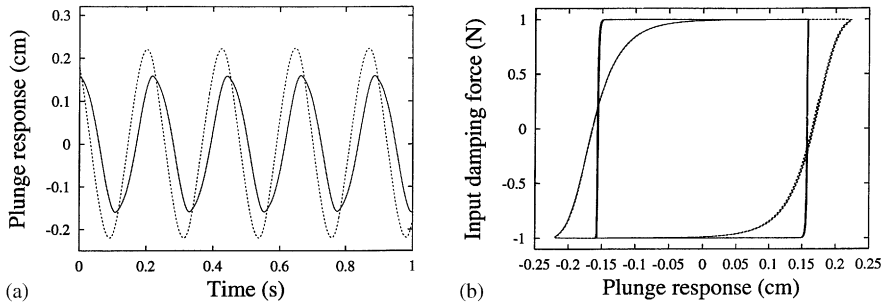


Fig. 10. Effect of damper parameters on plunge gust response at $\omega = 4.5$ Hz for $f_d = 1$ N: (a) for plunge response and (b) for hysteretic behavior; —, $d_0 = 0.024$ cm, $v_0 = 0.13$ cm/s; ⋯, $d_0 = 0.08$ cm, $v_0 = 2.2$ cm/s.

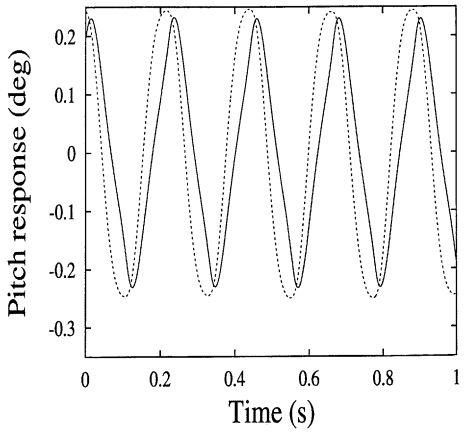


Fig. 11. Effect of damper parameters on pitch gust response at $\omega = 4.5$ Hz for $f_d = 1$ N: —, $d_0 = 0.024$ cm, $v_0 = 0.13$ cm/s; ⋯, $d_0 = 0.08$ cm, $v_0 = 2.2$ cm/s.

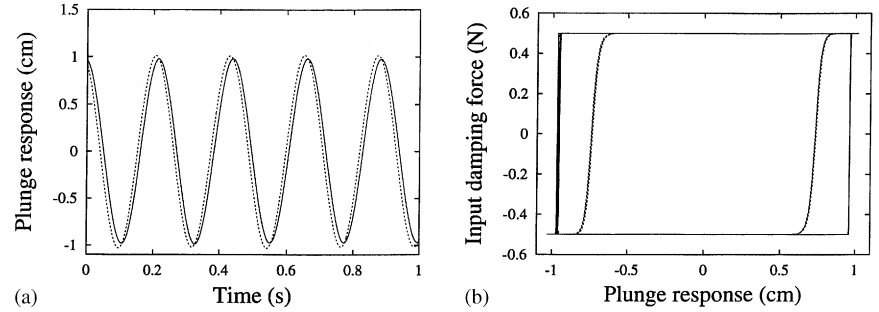


Fig. 12. Effect of damper parameters on plunge gust response at $\omega = 4.5$ Hz for $f_d = 0.5$ N: (a) for plunge response and (b) for hysteretic behavior; —, $d_0 = 0.024$ cm, $v_0 = 0.13$ cm/s; ⋯, $d_0 = 0.08$ cm, $v_0 = 2.2$ cm/s.

### 5.4. Non-linear response to two harmonic gust load (Case 2)

The gust generator installed in the Duke University low speed wind tunnel provides a two harmonic gust load although the second harmonic component is small. In this numerical study,

the continuous periodic gust is expressed as

$$w_g(t) = \bar{w}_{gs1} \sin \omega t + \bar{w}_{gs2} \sin(2\omega t + \Delta\phi), \tag{15}$$

where $\omega, \bar{w}_{gs1}$ are the main gust excitation frequency and peak gust velocity and $\bar{w}_{gs2}, \Delta\phi$ are the second peak gust velocity and the phase angle between the main and second components gust velocities. The main peak gust angle of attack is $\alpha_g = 1^\circ$ and the lateral main peak gust velocity is $\bar{w}_{gs1} = U\alpha_g/57.3$. The second peak gust velocity is assumed to be $0.2\bar{w}_{gs1}$. The measured phase angle $\Delta\phi$ has a random behavior around a mean of zero due to the tunnel turbulence. Here a random average is taken, i.e., $\Delta\phi = 0$.

Fig. 13 shows the plunge, pitch and flap rotation r.m.s. amplitude vs. the gust excitation frequency. As shown in Fig. 13(a), the plunge resonant frequency is 4.58 Hz. When no EMD damper is included in the system, i.e., $f_d = 0$, the plunge resonant r.m.s. amplitude is 1.1 cm, the corresponding pitch r.m.s. amplitude is 1.2° and the flap rational angle is 0.68° as shown in Figs. 13(b) and (c), respectively. The results are the same as shown in Fig. 7. It is interesting to find there is a second significant peak amplitude at the half plunge resonant frequency. This is due to the second harmonic gust component excitation. The r.m.s. response amplitude is about 0.4 cm for plunge, 0.4° for pitch and 0.25° for flap. The pitch resonant frequency is 7.4 Hz and flap resonant frequency is 17 Hz. When $f_d = 0.5$ N, the plunge resonant frequency has a slight increase, but the r.m.s. amplitude decreases to 0.7 cm though it is higher than that for the single harmonic gust excitation (0.59 cm). The peak amplitude at the half plunge resonant frequency obviously decreases. The corresponding pitch and flap responses are also decreased at this frequency from 1.2° to 0.9° (0.67° for a single harmonic gust) and 0.68° to 0.48° (0.37° for a single

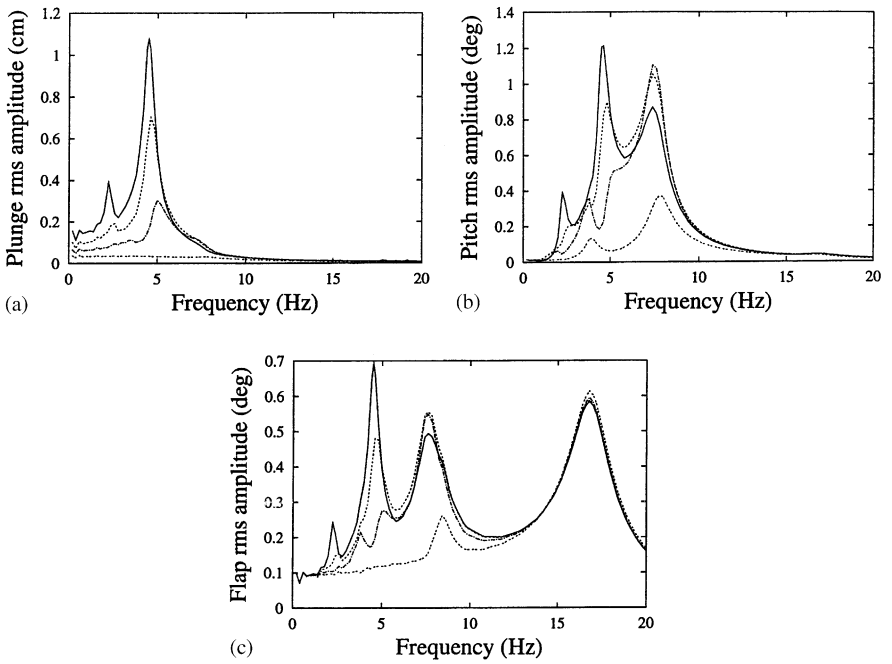


Fig. 13. R.m.s. frequency response vs. the gust excitation frequency for two harmonic gust excitation: (a) for plunge, (b) for pitch and (c) for flap response; —, $f_d = 0$ N; ···, $f_d = 0.5$ N; ---, $f_d = 1.0$ N; - -, $f_d = 2.00$ N.

harmonic gust). Unfortunately, at the pitch resonant frequency the r.m.s. amplitude increases both for the pitch and flap responses. When $f_d = 1.0$ N, the plunge response has been significantly alleviated in the dominant resonant range for the single harmonic gust excitation, but not for the two harmonic gust excitation. The plunge response still has an obvious peak at $\omega = 5$ Hz even though the r.m.s. amplitude is only 0.3 cm. The corresponding pitch and flap responses are similar to the results for $f_d = 0.5$ N. When $f_d = 2.0$ N, the plunge frequency response is almost flat with very small r.m.s. amplitude. The pitch resonant frequency has slightly increased, i.e., from 7.4 to 7.8 Hz. There is a second significant peak amplitude at half of the pitch resonant frequency. It is also due to the second harmonic gust component excitation. The flap peak responses disappear at frequencies, 3.8, 5 and 7.4 Hz for $f_d = 1.0$ N and a new flap peak response is created at half of the flap resonant frequency. This means that the present structural system has only pitch and flap degrees of freedom, and the plunge motion "sticks".

Fig. 14 shows the plunge time histories (a) and FFT analysis (b) for a fundamental gust excitation frequency, 2.25 Hz, for several EMD damping force levels. For $f_d = 0$, the response motion includes two harmonic components with a main gust frequency, 2.25 Hz and a second harmonic gust frequency, 4.5 Hz (note that the latter is very near the plunge natural frequency). As seen from the FFT plot, although the fundamental gust frequency is 2.25 Hz, the response is dominated by 4.5 Hz, the second harmonic gust frequency. As the damping force level increases, the response obviously decreases and the motion becomes more complex. This is because the damping force is non-linear (dry friction behavior). An interesting result is that the harmonic frequencies of the non-linear damping force are multiples of the fundamental gust frequency as shown in Fig. 15. Fig. 15(a) is the time history of the non-linear damping force and Fig. 15(b) is the corresponding FFT for gust excitation at the fundamental gust frequency, 2.25 Hz, for several EMD damping force levels. The strong non-linear damping force leads to a non-linear aeroelastic response.

From the above theoretical analysis, it is found that the damping device provides different contributions to the dynamic system for different gust excitation frequencies. One can define an alleviation ratio, $\eta_f$, for the frequency response to a periodic gust, as

$$\eta_f = \int_{\omega_0}^{\omega_m} x_{nonlinear}(\omega)\,\mathrm{d}\omega \Big/ \int_{\omega_0}^{\omega_m} x_{linear}(\omega)\,\mathrm{d}\omega, \tag{16}$$

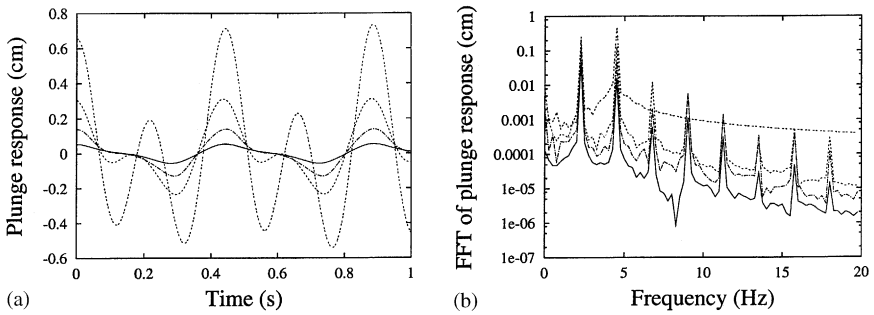


Fig. 14. Plunge response and FFT analysis for $\omega = 2.25$ Hz: (a) for plunge response at $\omega = 2.25$ Hz and (b) for FFT analysis; - -, $f_d = 0$ N; ···, $f_d = 0.5$ N; ---, $f_d = 1.0$ N; —, $f_d = 2.00$ N.

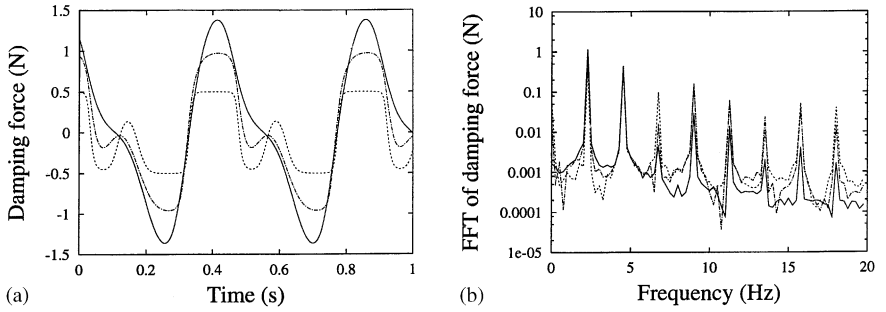


Fig. 15. Nonlinear damping force response and FFT analysis for $\omega = 2.25$ Hz: (a) for damping force at $\omega = 2.25$ Hz, and (b) for FFT analysis; —, $f_d = 2$ N; ---, $f_d = 1.0$ N; ···, $f_d = 0.5$ N.

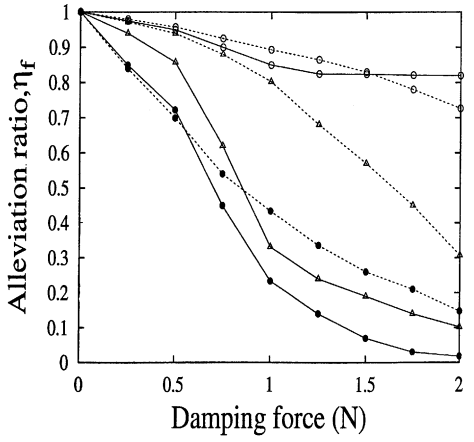


Fig. 16. Alleviation ratio, $\eta_f$, for the frequency response to a single and a two harmonic gust excitations. Case 1: –○–, flap; –△–, pitch; –●–, plunge. Case 2: · · ○ · ·, flap; · · △ · ·, pitch; · · ● · ·, plunge.

where $x_{nonlinear}(\omega)$ is the non-linear frequency response r.m.s. amplitude (plunge or pitch or flap) as obtained from the aeroelastic model with an EMD damper, and $x_{linear}(\omega)$ is the frequency response r.m.s. amplitude as determined from the linear model without an EMD damper. $m$ is a total sample frequency number; here $m = 100$ and $\omega_0 = 0.1$ Hz, $\omega_m = 20$ Hz.

The theoretical results are shown in Fig. 16 for both the single and the two harmonic gust load. The plunge response alleviation is very evident. The pitch response alleviation is moderate. Although there is local maxima at some gust frequencies, the average frequency response over the gust frequency band still decreases as the damping force level increases. The flap response alleviation is slight.

It is also found that the response alleviation ratio, $\eta_f$, is greater for Case 2 than for Case 1. Note that Case 1 is defined as a single harmonic gust excitation and Case 2 as a two harmonic gust excitation, and the fundamental gust excitation amplitude is the same, $\alpha = 1^\circ$. This result can be explained as follows. Since the area within the hysteresis loop corresponds to the energy, $W$, dissipated in the dry friction damper per one cycle of the plunge displacement, an equivalent damping coefficient, $C_{eq}$, can be determined from the following equation (assuming a sinusoidal

plunge motion):

$$C_{eq} = W \Big/ \int_0^{2\pi/\omega} (\dot{h})^2 \, \mathrm{d}t, \tag{17}$$

and thus,

$$C_{eq} = \frac{W}{\pi\omega(h_s)^2},$$

where $h_s$ is the plunge amplitude and $\omega$ is the plunge frequency.

From this equation it is found the equivalent damping coefficient decreases as the plunge amplitude increases. The response amplitude for Case 2 is larger than that for Case 1 due to an additional second harmonic gust excitation in Case 2. Therefore the equivalent damping coefficient decreases, i.e., the damper provides less damping to the aeroelastic system in Case 2.

### 5.5. Non-linear response to a sweep frequency gust load

The nominal theoretical lateral peak gust angle of attack, $\alpha_g$, is chosen to be $1^\circ$ for a continuous linear frequency sweep gust load. The minimum and maximum frequencies are 0 and 40 Hz, and the sweep duration $T$ is 3.2 s. The initial conditions are set to zero for all time simulations.

To depict concisely the non-linear response to the sweep frequency gust, an average PSD analysis can be used. Here, 10 PSD time simulation realizations are taken. More than 10 PSD realizations do not change the averaged results significantly.

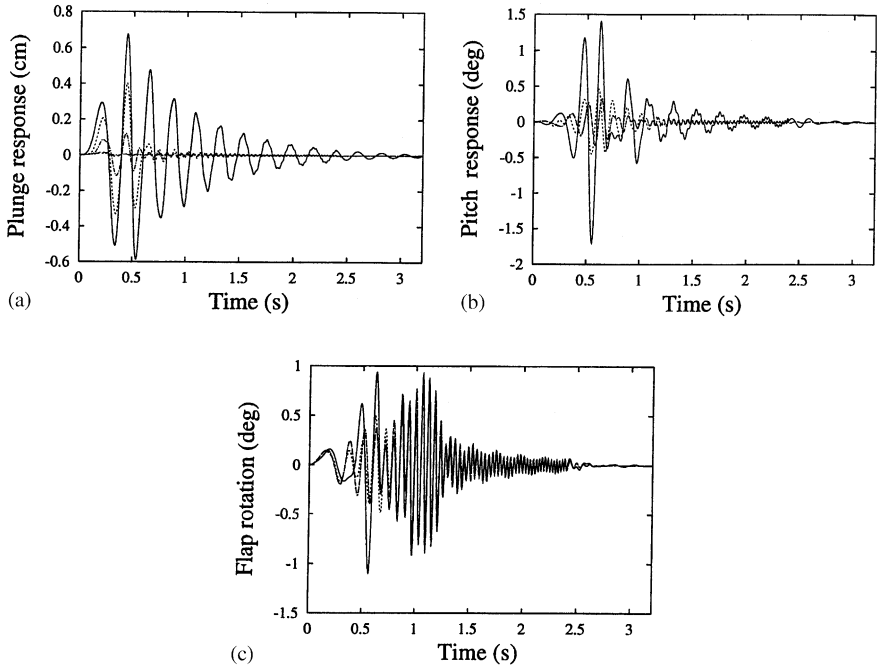


Fig. 17. Gust response to a sweep frequency gust for $\alpha_g = 1^\circ$: (a) for plunge, (b) for pitch and (c) for flap; —, $f_d = 0$ N; ···, $f_d = 0.5$ N; ---, $f_d = 1.0$ N; - -, $f_d = 2.00$ N.

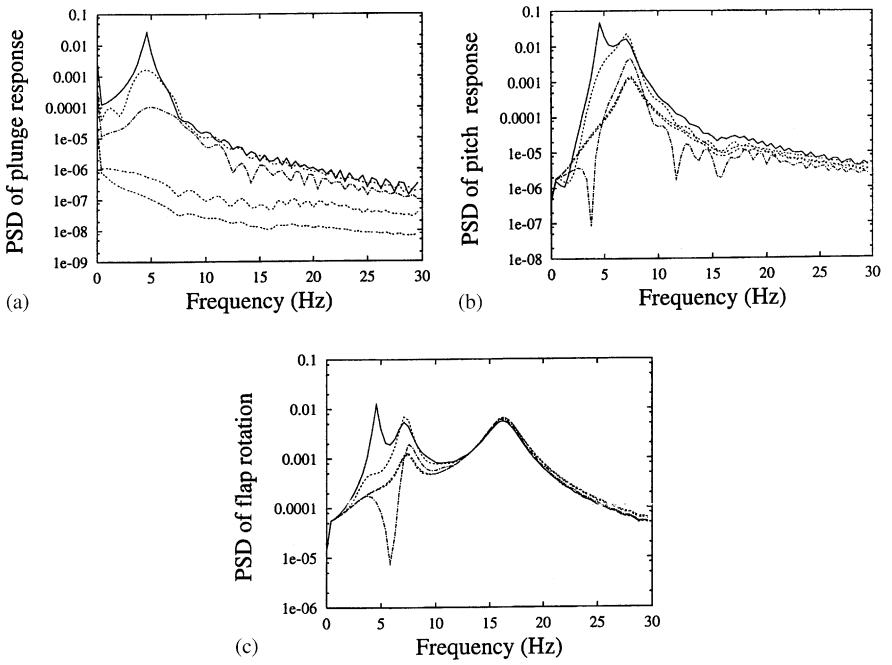


Fig. 18. Averaged PSD analysis for a sweep frequency gust for $\alpha_g = 1^\circ$: (a) for plunge, (b) for pitch and (c) for flap; —, $f_d = 0$ N; ⋯, $f_d = 0.5$ N; ---, $f_d = 1.0$ N; - -, $f_d = 1.5$ N; - - - , $f_d = 2.00$ N.

Firstly, linear system results are examined without the EMD damper, $f_d = 0$. The results are shown in Figs. 17 and 18 as indicated by the solid line. Fig. 17 shows the plunge, pitch and flap rotation time histories and Fig. 18 shows the corresponding PSD analysis for $U = 18$ m/s. From Fig. 18 we find the three resonant frequencies are 4.58, 7.4 and 17 Hz which are very close to the system natural frequencies. Due to an increased aerodynamic stiffness, the first aeroelastic natural frequency (dominated by plunge motion) is higher than the first structural natural frequency (4.07 Hz) in vacuo.

The results for several different dry friction damping levels are also plotted in the Figs. 17 and 18. The plunge and pitch gust responses significantly decrease as the damping level increases. However, the flap rotation is almost independent of the damping force. The frequency response behavior for a sweep frequency gust load is very similar to those for a single harmonic gust load except for the response amplitude.

Fig. 19 shows the averaged PSD for an air speed of $U = 18$ m/s, $f_d = 0.5$ N and several different gust strengths, $\alpha_g = 0.5^\circ$, $1^\circ$ and $2^\circ$. For the smaller larger gust strengths, $\alpha_g = 0.5^\circ$ the structural responses are significantly alleviated. However, for the larger gust strengths, $\alpha_g = 2.0^\circ$, the damping force $f_d = 0.5$ N is not enough to alleviate the structural responses.

The effects of the EMD damper parameters on the gust response are also considered in the sweep frequency gust. The damper parameters considered are $v_0 = 0.13$ cm/s, $d_0 = 0.024$ cm or $v_0 = 2.2$ cm/s, $d_0 = 0.08$ cm. Fig. 20 shows the averaged PSD using the two sets of the damper parameters for $f_d = 1$ N. The response amplitude increases for the latter damper parameters. This is because these damper parameters provide less dry friction force in a sweep cycle.

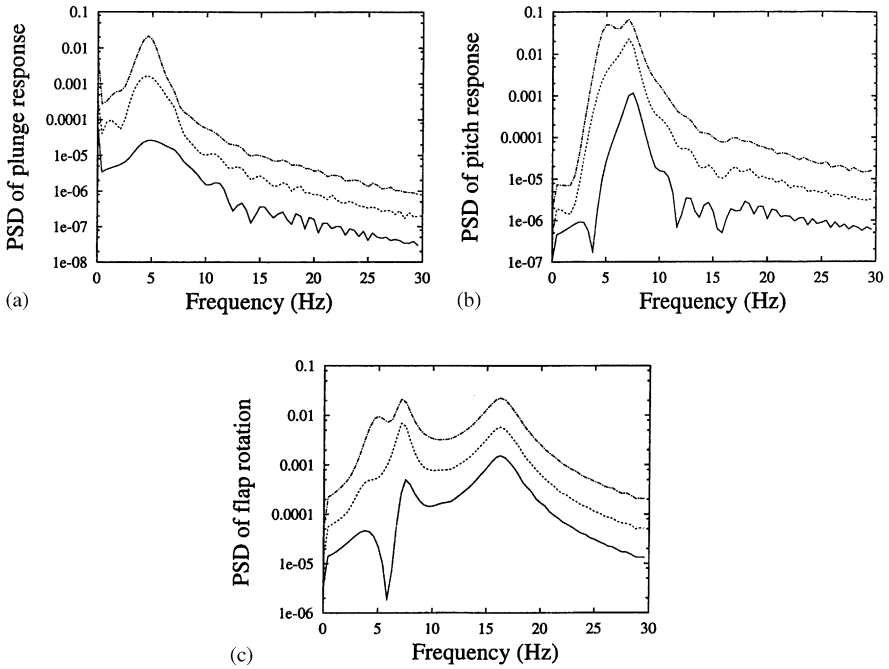


Fig. 19. Averaged PSD analysis for the damping force $f_d = 0.5$ N and $\alpha_g = 0.5°, 1°, 2°$: (a) for plunge, (b) for pitch and (c) for flap; —, $\alpha_g = 0.5°$; ⋯, $\alpha_g = 1.0°$; ---, $\alpha_g = 2.0°$.

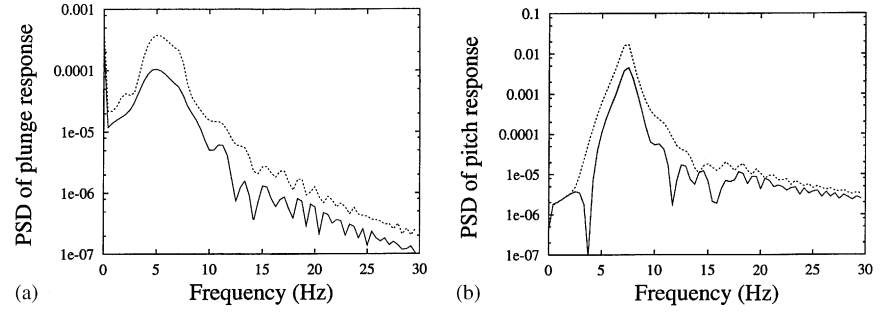


Fig. 20. Effect of damper parameters on response for a sweep frequency gust and for $f_d = 1.0$ N: (a) for plunge PSD and (b) for pitch PSD; —, $d_0 = 0.024$ cm, $v_0 = 0.13$ cm/s; ⋯, $d_0 = 0.08$ cm, $v_0 = 2.2$ cm/s.

When the damping force amplitude, $f_0$ decreases from $f_d = 1$ to 0.5 N, the effect of the EMD damper parameter on the gust response decreases. The results are shown in Fig. 21.

One can define an alleviation ratio, $\eta_t$, for the time response to a sweep frequency gust, as

$$\eta_t = \sqrt{\frac{1}{m_t}\sum_{i=1}^{m_t} x_{i,nonlinear}^2} \Bigg/ \sqrt{\frac{1}{m_t}\sum_{i=1}^{m_t} x_{i,linear}^2}, \tag{18}$$

where $x_{i,nonlinear}$ is the non-linear time response (plunge or pitch or flap) as obtained from the aeroelastic model with an EMD damper, and $x_{i,linear}$ is the time response as determined from the

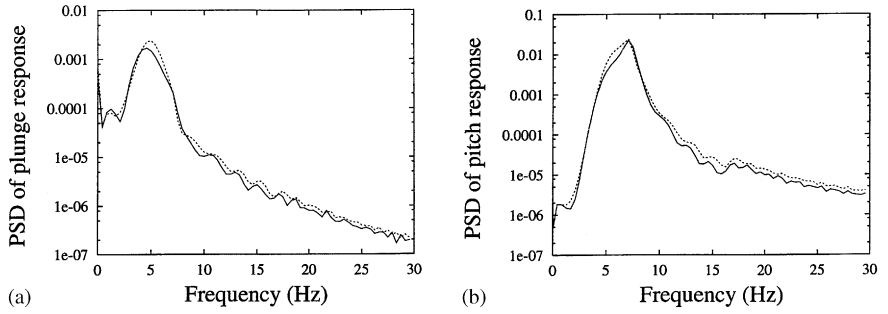


Fig. 21. Effect of damper parameters on response for a sweep frequency gust and for $f_d = 0.5$ N: (a) for plunge PSD and (b) for pitch PSD; —, $d_0 = 0.024$ cm, $v_0 = 0.13$ cm/s; ⋯, $d_0 = 0.08$ cm, $v_0 = 2.2$ cm/s.

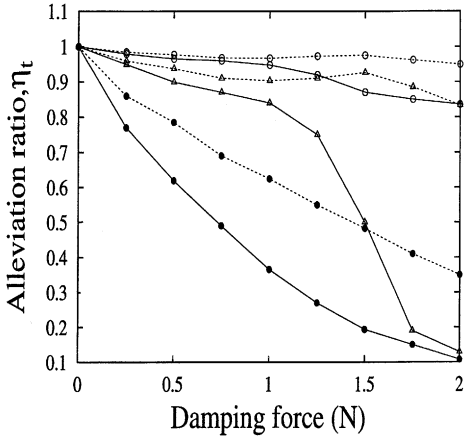


Fig. 22. Alleviation ratio, $\eta_t$, for the time response to a sweep frequency gust for $\alpha_g = 1^\circ$ and $2^\circ$. $1^\circ$: –○–, flap; –△–, pitch; –●–, plunge. $\alpha_g = 2^\circ$: · · ○ · ·, flap; · · △ · ·, pitch; · · ● · ·, plunge.

linear model without an EMD damper. The number, $m_t$, is a total sample number (time series number); here $m_t = 5120$.

The theoretical results for the gust loads, $\alpha_g = 1^\circ$ and $2^\circ$ are shown in Fig. 22. The plunge and pitch response alleviations are very evident. The flap response alleviation is slight. It is also seen that the response alleviation is less efficient when the gust load increases from $\alpha_g = 1^\circ$ to $2^\circ$. The reason is the same as described in the explanation of Fig. 16. A larger gust load leads to a larger response amplitude and the dry friction damper provides a smaller equivalent hysteresis damping.

## 6. Conclusions

An electro-magnetic, controllable dry friction damper has been designed and numerically simulated. The non-linear gust response of a three d.o.f. typical airfoil section with a control surface using this non-linear damper has been studied theoretically. Results for both a periodic and a linear frequency sweep gust excitations show that the present electro-magnetic dry friction damper can be used to alleviate the gust response, especially for the plunge and pitch responses.

## Acknowledgements

This work was supported by an AFOSR Grant "Dynamics and Control of Nonlinear Fluid–Structure Interaction" under the direction of Dr. Dean Mook. All numerical calculations were done on a supercomputer in the North Carolina Supercomputing Center (NCSC).

## Appendix A. Nomenclature

| | |
|---|---|
| $a$ | position of pitch hinge |
| $b$ | semi-chord of the airfoil section |
| $c$ | position of flap hinge |
| $C_h, C_\alpha, C_\beta$ | structural damping coefficients for $h, \alpha, \beta$ generalized co-ordinates |
| $f_D$ | damping force from EMD damping device |
| $h$ | plunge displacement |
| $I$ | input current |
| $I_\alpha, I_\beta$ | moments of inertia per unit span of wing–aileron and aileron about a and c, respectively |
| $K_h, K_\alpha, K_\beta$ | structural stiffness coefficients for $h, \alpha, \beta$ generalized co-ordinates |
| $l$ | span length of the airfoil |
| $L$ | lift force |
| $M_\alpha$ | aerodynamic moment about the midchord |
| $M_\beta$ | aerodynamic moment about the flap axis |
| $M_r$ | reference mass/length of wing–aileron system |
| $n$ | inflow expansion index |
| $N$ | number of inflow states |
| $p$ | aerodynamic pressure |
| $q$ | aerodynamic modal co-ordinate |
| $t$ | time |
| $U$ | airspeed |
| $U_f$ | flutter airspeed |
| $w_g(x, t)$ | lateral gust velocity |
| $w_{gn}$ | expansion coefficients of $w_g(x, t)$ |
| $\bar{w}_{gs}$ | amplitude of sinusoidal gust |
| $x$ | streamwise co-ordinate |
| $y$ | co-ordinate normal to $x$ |
| $\alpha$ | torsional angle or pitch rotation of wing |
| $\alpha_g$ | gust angle of attack |
| $\beta$ | flap rotational angle |
| $\eta_t, \eta_f$ | gust response alleviation ratio for frequency sweep and periodic gust excitation, respectively |
| $\lambda$ | induced flow due to free vorticity |
| $\lambda_n$ | expansion coefficients for $\lambda$ |

| | |
|---|---|
| $\rho$ | air density |
| $\omega$ | gust excitation frequency |
| $\omega_h, \omega_\alpha, \omega_\beta$ | uncoupled plunge, torsional and flap natural frequencies, respectively |
| $(\dot{})$ | $\mathrm{d}()/\mathrm{d}t$. |

## References

[1] S.B. Choi, Y.T. Choi, D.W. Park, A sliding mode control of a full-car ER suspension via hardware-in the-loop-simulation, Journal of Dynamic Systems, Measurement and Control 122 (2000) 114–123.
[2] J.D. Carlson, J.L. Sproston, Controllable fluid in 2000-status of ER and MR fluid technology, Seventh International Conference on New Actuators, 19–21 June, Bremen, Germany, 2000.
[3] H.P. Gavin, Implementation and modeling of a semi-active control system, in: F. Ansari (Ed.), Condition Monitoring of Materials and Structures, American Society of Civil Engineers, Reston, VA, 1999.
[4] X. Tang, X. Zhang, R. Tao, Flexible fixture device with magneto-rheological fluids, Journal of Intelligent Material Systems and Structures 10 (9) (1999) 690–694.
[5] D.Y. Lee, N.M. Wereley, Quasi-steady Herschel-Bulkley analysis of electro- and magneto-rheological flow mode dampers, Journal of Intelligent Material Systems and Structures 10 (10) (1999) 761–769.
[6] W.I. Kordonsky, Magneto-rheological effect as a base of new devices and technologies, Journal of Magnetism and Magnetic Materials 122 (1–3) (1993) 395–398.
[7] B.F. Spencer, S.J. Dyke, M.K. Sain, J.D. Carlson, Phenomenological model for magnetorheological dampers, Journal of Engineering Mechanics 123 (3) (1997) 230–238.
[8] N.M. Wereley, G.M. Kamath, V. Madhavan, Hysteresis modeling of semi-active magnetorheological helicopter dampers, Journal of Intelligent Material Systems and Structures 10 (8) (1999) 624–633.
[9] S.P. Kelso, F. Gordaninejad, Magnetorheological fluid shock absorbers for off-highway high-payload vehicles, SPIE Proceedings Series 3672 (1999) 44–45.
[10] F. Gordaninejad, S.P. Kelso, Fail-safe magneto-rheological fluids dampers for off-highway high-payload vehicles, Journal of Intelligent Material Systems and Structures 11 (5) (2000) 395–406.
[11] H.P. Gavin, J. Hoagg, M. Dobossy, Optimal design of MR dampers, Proceedings of the US–Japan Workshop on Smart Structures for Improved Seismic Performance in Urban Regions, August, Seattle, WA, 2001, pp. 225–236.
[12] Z.C. Yang, L.C. Zhao, Chaotic motions of an airfoil with nonlinear stiffness in incompressible flow, Journal of Sound and Vibration 138 (2) (1990) 245–254.
[13] E.H. Dowell, D.M. Tang, Nonlinear aeroelasticity and unsteady aerodynamics, Von Karman Lecture presented at the 2002 Aerospace Sciences Meeting, Reno, Nevada, AIAA Paper, 2002, pp. 2002–0003.
[14] D.A. Peters, Finite-state airloads for deformable airfoils on fixed and rotating wings, Symposium on Aeroelasticity and Fluid/Structure Interaction, ASME Winter Annual Meeting, Chicago, November, Revision 3, May 1996, 1994.
[15] M.D. Conner, D.M. Tang, E.H. Dowell, L.N. Virgin, Nonlinear behavior of a typical airfoil section with control surface freeplay: a numerical and experimental study, Journal of Fluids and Structures 11 (1) (1997) 89–101.
[16] E.H. Dowell, E.F. Crawley, H.C. Curtiss Jr., D.A. Peters, R.H. Scanlan, F. Sisto (Eds.), A Modern Course in Aeroelasticity, 3rd Edition, Kluwer Academic, Dordrecht, 1995, pp. 193–227.
[17] D.M. Tang, D. Kholodar, E.H. Dowell, Nonlinear response of a typical airfoil section with control surface freeplay to gust loads, American Institute of Aeronautics and Astronatics Journal 38 (9) (2000) 1543–1557.
[18] D.A. Peters, W.M. Cao, Finite state induced flow models, Part I: two-dimensional thin airfoil, Journal of Aircraft 32 (2) (1995) 313–322.